J. Martínez, F. Piscaglia, A. Montorfano, A. Onorati, S.M. Aithal
Influence of Spatial Discretization Schemes on Accuracy of Explicit LES: Canonical Problems to Engine-Like Geometries
Computers & Fluids, Vol. 117, 2015, p. 62-78
doi:10.1016/j.compfluid.2015.05.007

Influence of spatial discretization schemes on accuracy of explicit LES: Canonical problems to engine-like geometries

J. Martínez[*,a], F. Piscaglia[a], A. Montorfano[a], A. Onorati[a], S.M. Aithal[b]

[a] *Dip. di Energia, Politecnico di Milano, Via Lambruschini 4, 20159, Milano-Italy*
[b] *Argonne National Laboratory, Lemont, IL 60439, United States*

Abstract

The choice of the spatial discretization scheme and the subgrid-scale (SGS) model can have a significant impact on the accuracy of Large Eddy Simulations (LES). A systematic study of the influence of the advection term discretization scheme, namely (`CDS`, `LUST`) and the SGS model (σ-model, WALE and dynamic Smagorinsky) on the accuracy of the solution is presented in this work. Three canonical cases with increasing complexity are considered in this study, namely, a fully developed turbulent channel flow with $Re_\tau = 395$, a backward facing step and a wall-mounted hump. Mean errors with respect to DNS or experimental data are quantified in order to compare the relative accuracy of each combination of scheme/model. Detailed comparison of the numerical simulations performed by the open-source CFD code OpenFOAM® shows that the σ-model with the `LUST` discretization scheme yields the best results. This combination of σ-model with `LUST` discretization scheme has hence been used to study the turbulent flow characteristics in an

[*]Corresponding author
Email address: `jmartrubio@gmail.com` (J. Martínez)

engine-like geometry. Results show good agreement with experimental data.
Key words: Engine LES, Sigma, OpenFOAM

1. Introduction

With the advent of low-cost large-scale computing, Computational Fluid Dynamics (CFD) has become one of the most commonly used tools in the study of turbulent flows. Powerful computers have enabled the development of complex models and algorithms to achieve meaningful results in a wide variety of situations. In the simulation of turbulent flows, Direct Numerical Simulations (DNS) and Reynolds Averaged Navier-Stokes simulations (RANS) represent the two extremes for turbulence modeling [1]. DNS is the most accurate and simplest approach from a conceptual point of view, as it consists of solving all scales contained in the flow without any averaging or approximation, thus incurring the highest computational cost (wall time and hardware resources such as processors and memory). On the other hand, RANS simulations solve for the mean flow with an appropriate model for the turbulent energy transfer among various scales. Reasonable computational cost and an acceptable accuracy make RANS modeling the most widely used approach. However, RANS does not solve for the unsteady flow structures, the intrinsic characteristic of turbulent flows, and indeed it may fail to reproduce relevant flow physics for many engineering problems. Large Eddy Simulation (LES) lies between the two extremes. LES is based on the numerical solution of large scales of fluid structures combined with modeling the effect of small-scale motions. The LES approach is based on the accepted notion that large-scale motions are highly affected by the geometry of the do-

main, while subgrid-scale motions can be considered similar and statistically isotropic. Hence in LES, large scale motion is explicitly simulated, while fluid motion at smaller scales (also known as subgrid-scales) are modeled by a subgrid-scale (SGS) model: as a consequence, LES allows for a more comprehensive insight of the flow characteristics and therefore yields more accurate predictions.

However, the use of SGS models has some inherent limitations. Even though recently proposed SGS models [2, 3, 4] attempt to reproduce the proper near-wall behavior ($\nu_{SGS} = O(y^3)$) without the necessity of additional wall-treatments [5, 6, 7, 8], mesh resolution requirements for wall-resolved LES are prohibitively large for industrial applications [9, 10, 11]. These applications are characterized by high Reynolds number flows and large complex geometries. Stringent near-wall grid spacing is required not only in the wall-normal direction ($y^+ \approx 1$), but also in the streamwise ($\Delta x^+ \approx 100$) and spanwise ($\Delta z^+ \approx 30$) directions [12].

For such applications, it is instructive to examine the accuracy and robustness of a subgrid-scale model when the stringent mesh resolution requirements are not completely satisfied. Simulation of turbulent flows in internal combustion engine geometries is one such illustrative example.

Furthermore, in cases characterized by strong gradients of physical quantities, or whenever a complex mesh is used, numerical discretization schemes are required to be at least locally dissipative in order to ensure numerical stability.

When numerical dissipation acts as a source term in the momentum equations, the SGS model is considered to be implicitly contained in the numerical

scheme; this case is referred to as the Implicit LES (ILES). In explicit LES, an ad-hoc SGS model is used to model the small turbulent scales; in this case, if dissipative schemes are used, their dissipation may be comparable to the SGS viscosity and, therefore, they may adversely affect the accuracy of the SGS model. Hence, the choice of the numerical scheme, particularly for advection terms, will significantly affect the performance of a given model.

The objective of the present study is to analyze the influence of spatial discretization schemes of advection terms on three subgrid-scale (SGS) models in a finite volume (FV) framework. A pure second order central differencing scheme (`CDS`) and a blended scheme Linear Upwind Stabilized Transport (`LUST`) [13] are considered in this study. The computational tool used is the open-source CFD software OpenFOAM®, which has been extensively developed by the authors for LES [14, 15, 16, 17, 18, 19, 20], including the Wall-Adapting Local Eddy-viscosity model [3] (WALE), the dynamic formulation of the Smagorinsky model [21] and most recently, the Sigma model [2] (σ-model).

Four cases were selected with this purpose: first, a fully developed turbulent channel flow with a perfectly orthogonal structured mesh was used to compare near-wall behavior of each of the models using `CDS` scheme. The second case was a single-sided expansion (Backward Facing Step) where, maintaining an orthogonal mesh, models were checked to properly reproduce the re-circulation region. For this case, the amount of numerical viscosity provided by the pure second order `CDS` scheme and by the blended `LUST` [13] scheme was studied by analyzing the influence on the computed flow features when different subgrid-scale models were applied. These SGS models were

also tested in a 2D wall-mounted hump with a non-orthogonal mesh which is representative of a more complex geometry. For this last case, only `LUST` scheme was used, as pure second order schemes can cause numerical instability. Based on the observations of these canonical cases, the most appropriate discretization scheme and SGS model was used to study a high-Reynolds number flow ($Re \approx 45{,}000$) in a complex engine-like geometry with a poppet valve. This case was selected as it is illustrative of high-Reynolds number complex geometry cases frequently encountered in industrial applications. These cases were chosen since they represent four cases of progressively increasing levels of complexity in terms of non-orthogonality of the mesh, that forces the use of limiters on spatial discretization. For each of the above mentioned cases, mean errors in important flow features (such as average velocity and velocity fluctuations) were determined for each model and compared with available DNS or experimental data.

2. The blended LUST scheme

For the benefit of the reader a simplified description of the blended `LUST` scheme used in this study is shown next. Linear Upwind Stabilized Transport refers to a group of spatial discretization schemes consisting of a blend between the centered linear interpolation (Central Differencing Scheme `CDS`) and the linear upwind (`LU`) scheme. Maintaining a second order accuracy, this kind of blend allows the reduction of the typical instabilities derived from the use of pure second order `CDS` schemes in complex meshes [13]. Since they are obtained from the blend of two linear accuracy schemes, `LUST` schemes are more accurate than blends of linear and first-order schemes (see for example

APVM scheme [22]).

To describe LUST schemes a two-dimensional grid is considered as shown in Fig. 1.

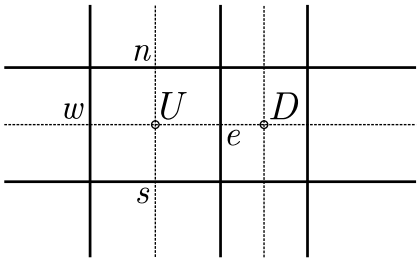

Fig. 1: Two dimensional grid to illustrate LUST schemes

U refers to the upwind cell while D is the downwind cell. Considering a property ϕ, the central differencing scheme (CDS) can be used to determine the value of the property at e as:

$$\phi_e^{CDS} = \lambda\phi_U + (1-\lambda)\phi_D \quad \text{where} \quad \lambda = \frac{|\mathbf{x}_D - \mathbf{x}_e|}{|\mathbf{x}_D - \mathbf{x}_U|} \tag{1}$$

λ and $(1-\lambda)$ are therefore the weighting factors when CDS is used.

The linear upwind interpolation (LU) is a Taylor-series expansion about the upwind cell center:

$$\phi_e^{LU} = \phi_U + (\mathbf{x}_e - \mathbf{x}_U) \cdot \nabla_U \phi \tag{2}$$

where $\nabla_U \phi$ is the gradient of ϕ at the center of the upwind cell, and can be calculated using Gauss's theorem with centered linear interpolation:

$$\nabla_U \phi = \frac{1}{A_U} \sum_f \phi_f^{CDS} d_f \mathbf{i}_f \tag{3}$$

where f refers to all edges of upwind cell U (n, s, e, w), d_f is the length of edge f, $\mathbf{i}_f$ is the outward-pointing unit normal to f and A_U is the area of

the upwind cell. In the implementation of the linear upwind interpolation scheme in OpenFOAM®, weighting factors are given by those of the first order upwind scheme (which corresponds to the first term in RHS of Eq. 2), while the gradient dependent term (second term in RHS of Eq. 2) is treated as an explicit correction. This explicit treatment increases both the stability and the numerical dissipation of the `LU` scheme at the cost of an increased error [23].

With this considerations, the blend `LUST` scheme can be defined as:

$$\phi_e^{LUST} = b\,\phi_e^{CDS} + (1-b)\,\phi_e^{LU} \tag{4}$$

The constant b was chosen to be equal to 0.75, according to H. Weller's recommendations [13]; as a consequence, blending was performed using 25% of contribution from linear upwind scheme and 75% from `CDS`. By blending `CDS` with a linear upwind scheme, stability is reinforced but a slightly higher numerical dissipation is introduced.

3. Subgrid-scale models

Large-eddy simulation is based on the low-pass spatial filtering of the turbulent motions with a mathematically well-established formalism. The application of the LES filtering operation to the incompressible Navier-Stokes equations yields the LES equations which need modeling for the system to be closed [12].

The eddy-viscosity assumption is largely used to model the subgrid-scale (SGS) tensor in LES, as it greatly reduces the modeling effort [12, 24]. A brief overview of the SGS models considered in this work is summarized below for the benefit of the reader.

For incompressible fluids, the SGS tensor can be written as follows (implicit summation rule for repeated indices is used):

$$\tau_{ij}^{SGS} - \frac{1}{3}\tau_{kk}^{SGS}\delta_{ij} = -2\nu_{SGS}\overline{S}_{ij} \tag{5}$$

where δ_{ij} is the Kronecker symbol, τ_{ij} is the subgrid-scale tensor, defined by:

$$\tau_{ij}^{SGS} = \overline{u_i u_j} - \overline{u}_i\overline{u}_j \tag{6}$$

$\overline{S}_{ij}$ is the rate-of-strain tensor:

$$\overline{S}_{ij} = \frac{1}{2}\left(\overline{g}_{ij} + \overline{g}_{ji}\right) \tag{7}$$

and $\overline{g}_{ij}$ is the velocity gradient tensor of the resolved scales, defined by:

$$\overline{g}_{ij} = \frac{\partial\overline{u}_i}{\partial x_j} \tag{8}$$

The over-bar denotes the filtering operation. From a simple dimensional analysis, the subgrid-scale viscosity can be written as:

$$\nu_{SGS} = (C_m\overline{\Delta})^2\overline{OP}_m(\overline{\mathbf{u}}) \tag{9}$$

where C_m is the constant associated with the model m, $\overline{\Delta}$ is the subgrid characteristic length-scale (in practice the cell size) and $\overline{OP}_m$ is a differential operator associated with the model acting on the resolved velocity field $\overline{\mathbf{u}}$.

For all the simulations considered, and in every model, characteristic length-scale $\overline{\Delta}$ will be the third power of the local cell volume.

The operator and model constant was defined for each model as follows:

The dynamic Smagorinsky model [21]**:**

By far the most classical operator is the strain rate, which leads to the Smagorinsky model [25]:

$$\overline{OP}_s = \sqrt{2\overline{S}_{ij}\overline{S}_{ij}} \tag{10}$$

Following Lilly's framework [26], the closure problem in the dynamic formulation is achieved by terms of an additional test filter $\widehat{\Delta}$ (usually $\widehat{\Delta} = 2\overline{\Delta}$), and the model constant can be computed resorting to a least squares approach as:

$$C_s^2 = \frac{1}{2}\frac{\langle L_{ij}M_{ij}\rangle^+}{\langle M_{ij}M_{ij}\rangle} \tag{11}$$

where L_{ij} is the modified Leonard tensor:

$$L_{ij} = \widehat{\overline{u}_i\overline{u}_j} - \widehat{\overline{u}}_i\widehat{\overline{u}}_j \tag{12}$$

and M_{ij} is directly related to the differential operator and reads:

$$M_{ij} = \widehat{\Delta}^2\widehat{\overline{OP}_s}\widehat{\overline{S}}_{ij} - \overline{\Delta}^2\widehat{\overline{OP}_s\overline{S}}_{ij} \tag{13}$$

In Eq. 11, $\langle\cdot\rangle$ denotes a stabilization method consisting of a local volume averaging, and superscript "+" represents a positive clipping of all negative values to zero. Even though some techniques were proposed with the aim of avoiding this nonphysical clipping [27, 28, 29], positive clipping was chosen for simplicity and to avoid any computational overhead [30].

Table 1 shows the mean percentage of cells where clipping is performed for the different test cases considered with the dynamic Smagorinsky model. These large numbers give an idea of the importance of the numerical issues related to the dynamic procedure.

Table 1: Mean percentage of cells where clipping is performed for each case

Case	Mesh	% Cells with clipping
Channel flow	Coarse	31 %
	Fine	32 %
BFS	Coarse only	36 %
Hump	Coarse only	43 %

The WALE model [3]**:**

$$\overline{OP_w} = \frac{\left(s_{ij}^d s_{ij}^d\right)^{3/2}}{\left(\overline{S}_{ij}\overline{S}_{ij}\right)^{5/2} + \left(s_{ij}^d s_{ij}^d\right)^{5/4}} \tag{14}$$

where s_{ij}^d is the trace-less symmetric part of the square of the velocity gradient tensor ($\overline{g}_{ji}^2 = \overline{g}_{ik} \cdot \overline{g}_{kj}$):

$$s_{ij}^d = \frac{1}{2}\left(\overline{g}_{ij}^2 + \overline{g}_{ji}^2\right) - \frac{1}{3}\overline{g}_{kk}^2 \delta_{ij} \tag{15}$$

The constant used for simulations was obtained from calibration on different kinds of problems [3] and was set to:

$$C_w = 0.58 \tag{16}$$

The Sigma model (σ-model) [2]**:**

$$\overline{OP_\sigma} = \frac{\sigma_3(\sigma_1 - \sigma_2)(\sigma_2 - \sigma_3)}{\sigma_1^2} \tag{17}$$

where σ_i are the square root of the eigenvalues of $\overline{\mathbf{g}}^T\overline{\mathbf{g}} = \overline{g}_{ki}\overline{g}_{kj}$ (which are positive since $\overline{\mathbf{g}}^T\overline{\mathbf{g}}$ is symmetric semi-definite positive) and they read $\sigma_1 \geq \sigma_2 \geq \sigma_3$. The model's constant was again obtained from calibration [2]:

$$C_\sigma = 1.35 \tag{18}$$

In order to provide a theoretical comparison of the described models, Table 2 shows some of the properties that can be directly derived from the operator used by each of the models, as already shown in [2]. In particular, the static Smagorinsky model was added to the Sigma and WALE models, since a general comparison with the dynamic Smagorinsky cannot be performed. It is desirable that a subgrid-scale model satisfies a series of properties; first of all, the differential operator of the model should tend to zero near a solid boundary following a third power law [31]. Besides the operator should be zero for any two-dimensional flow, including solid rotation, pure shear, and axisymmetric/isotropic contraction/expansion.

As it can be inferred from Table 2 the Sigma model is the only one that theoretically behaves properly in all considered circumstances. Even though it has not been shown in the table, both the Sigma and WALE models always generate a positive value of SGS viscosity (backscatter phenomenon could justify a negative value, but this would imply stability issues). One problem associated with static models like the WALE and Sigma models, is the choice of the model coefficient which in general, needs to be calibrated for every particular case since results might be sensitive to this constant. In comparison, a dynamic procedure, despite its higher complexity, solves the problem of adapting the model constant to the mesh refinement. However, as commented in the case of the dynamic Smagorinsky model, the dynamic procedure could lead to negative values that would eventually generate instabilities, an issue that needs to be addressed.

Table 2: Properties of the SGS models considered. Values shown in the table are those obtained by the differential operator of each of the models when all velocity derivatives are zero excepting: Solid rotation: $\partial u_1/\partial x_2 = -1$ and $\partial u_2/\partial x_1 = 1$; Pure shear: $\partial u_1/\partial x_2 = 1$; Axisymmetric compression/expansion: $\partial u_1/\partial x_1 = \pm 2$, $\partial u_2/\partial x_2 = \mp 1$, $\partial u_3/\partial x_3 = \mp 1$; Isotropic compression/expansion: $\partial u_1/\partial x_1 = \pm 1$, $\partial u_2/\partial x_2 = \pm 1$, $\partial u_3/\partial x_3 = \pm 1$

Model	Smagorinsky	WALE	Sigma
Asymptotic behavior near the wall	$O(y^0)$	$O(y^3)$	$O(y^3)$
Solid rotation	0	≈ 0.904	0
Pure shear	1	0	0
Axisymmetric compression/expansion	$\approx$3.464	$\approx$0.151	0
Isotropic compression/expansion	$\approx$2.450	0	0

4. Numerical experiments

A widely-accepted approach in the validation of turbulence models is the use of nominally two-dimensional cases to compare predictions with reliable DNS or experimental data sets. In this work, four cases were considered: a fully developed turbulent channel flow, a backward facing step geometry, a 2D wall-mounted hump and an engine-like geometry with a poppet valve. As explained earlier, these cases represent progressively increasing levels of complexity in terms of non-orthogonality of the mesh and are thus useful in

evaluating the use of limiters on spatial discretization schemes.

In all cases low subsonic incompressible conditions apply. In this work, the original theory of the Sigma model [2] was implemented in the OpenFOAM® code. While the Sigma model might not show a significant improvement when compared to the WALE [3] and dynamic Smagorinsky [21] models for some benchmark problems, it was implemented because it is currently considered one of the best performing models [32, 33, 34, 35] when applied to LES of Internal Combustion (IC) Engines. The Sigma model was used to simulate the engine-like geometry considered in this work, comparing numerical results with experimental data.

For all cases, pressure-velocity coupling was solved by a PIMPLE (merged PISO-SIMPLE) algorithm, where convergence of pressure-velocity is enforced by iterating the coupling procedure for each time-step. Description of the PIMPLE procedure and its application to non-conformal grids can be found in [20]. All the simulations were carried out with a dynamic adjustment of the time-step on the basis of the limitation applied to the maximum CFL number allowed, that was set to 5. Implicit time-marching was used in all the simulations and time derivatives were discretised by a second-order backward approximation.

For post-processing of the results, statistical moments of first and second order (mean velocity field or Reynolds stress components for instance) were directly computed from the resolved fields without considering the additional contribution of unresolved scales. Even though several methods are found in literature to evaluate subgrid-scale contributions [36, 37, 38], it is generally true that statistical moments are essentially related to scale ranges contained

in the resolved field. Besides, uncertainties present in the techniques used for subgrid-scale contribution evaluation makes the direct comparison of resolved quantities and reference data a very common practice [12].

4.1. Turbulent channel flow

The first case considered was one of the simplest wall-bounded turbulent flows, the flow in a plane channel. The simulations were carried out at $Re_\tau = u_\tau h/\nu = 392.24$, where u_τ and h refer respectively to friction velocity and channel half-width. For comparison among models, reference values were taken from the work by R. D. Moser [39].

4.1.1. Computational procedure for Channel flow case

Periodic boundary conditions were applied in the streamwise (x) and spanwise (z) directions. The computational domain is shown in Fig. 2.

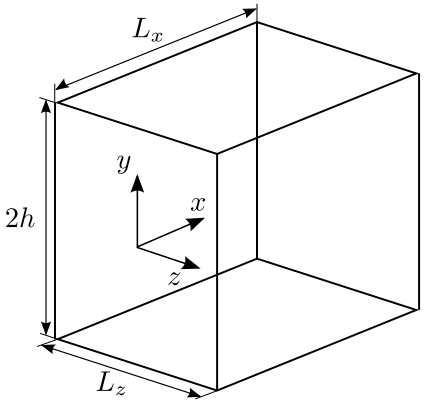

Fig. 2: Geometry considered for channel flow simulations; $L_x = 3.5h$; $L_z = 1.3h$.

Two meshes were considered (with 207,000 and 675,000 cells respectively) with the resolution shown in Table 3. The mesh was stretched in the wall

normal direction by using a geometric progression with a ratio of 1.06 (coarse mesh) and 1.003 (fine mesh).

Table 3: Number of grid cells and grid spacing in classical wall units.

Mesh	$N_x \times N_y \times N_z$	Δx^+_{max}	Δy^+_{max}	Δz^+_{max}
Coarse	$30 \times 138 \times 50$	80	1	15
Fine	$45 \times 200 \times 75$	25	0.1	5

Periodic domain sizes were selected to minimize two-point correlations in streamwise and spanwise directions. Two options were considered for the pressure gradient that drives the flow: either a fixed pressure gradient, or a variable gradient dynamically adjusted to maintain a constant mass flux through the channel.

Advection terms were discretized using a pure second-order differencing scheme, `CDS`. Convergence for flow statistics was checked by examining the symmetry of profiles over the channel height. Simulations were performed for all the SGS models previously introduced: Sigma, WALE, dynamic Smagorinsky and ILES.

4.1.2. Results for Channel flow

Velocity profiles are shown in Fig. 3 in classical wall units. As displayed, all LES mean velocity profiles are in good agreement with the reference data from available DNS studies. The largest difference is seen with the dynamic Smagorinsky model, for which the clipping of negative values in the calculated subgrid-scale viscosity (required for convergence) could have a negative influence on the results. Both WALE and Sigma models lead to an improve-

ment in results, showing a very similar prediction of velocity fields.

For the RMS-velocity profiles shown in Fig. 4, the Sigma and WALE models capture the peak of axial velocity fluctuations near the wall, while they show a slight under-estimation in the profiles of wall-normal and spanwise fluctuations (v^+_{rms} and w^+_{rms}). Overall, all the models, including the dynamic Smagorinsky behave in a similar manner.

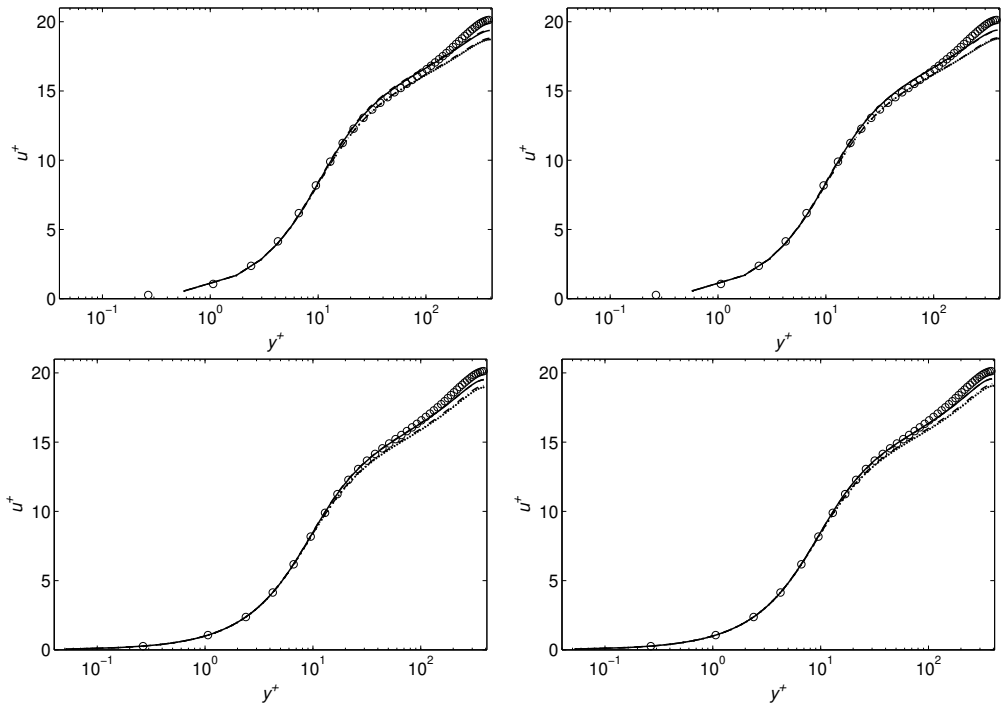

Fig. 3: Mean-velocity profiles in coarse (top) and fine mesh (bottom) for σ-model (—), dynamic Smagorinsky model ($- \cdot -$), WALE model (- - -) and ILES ($\cdots$), in comparison with DNS data ($\circ\circ\circ$) for fixed pressure gradient (left) and fixed mass flux (right).

In order to perform a numerical comparison between models, an error analysis methodology was proposed. Two variables were considered, mean streamwise velocity and turbulent kinetic energy.

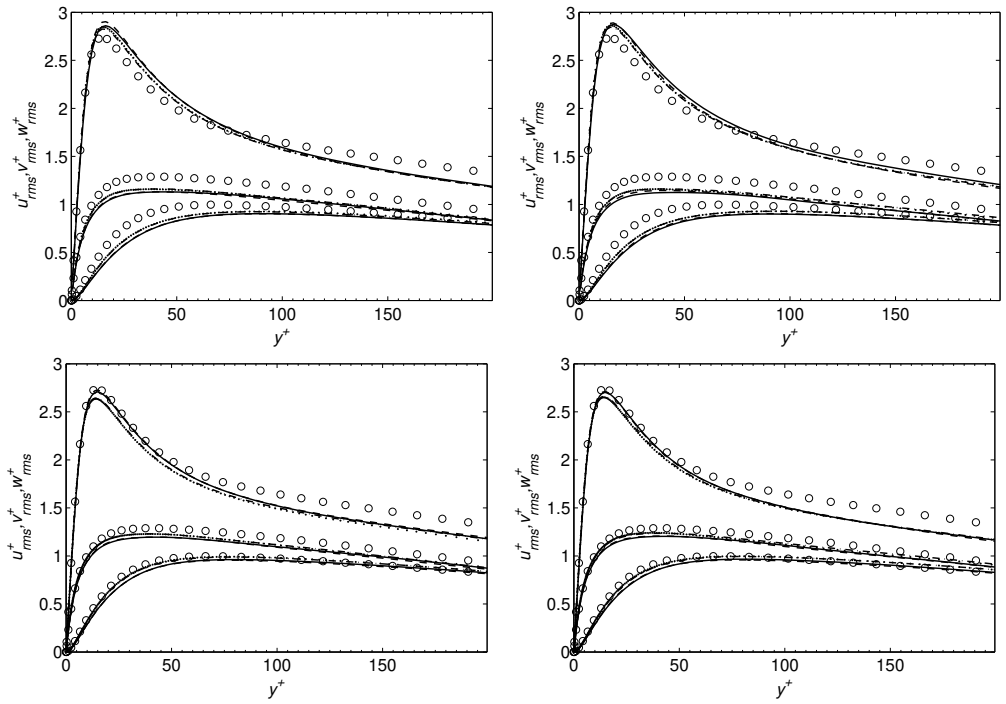

Fig. 4: RMS-velocity profiles in coarse (top) and fine mesh (bottom) for σ-model (—), dynamic Smagorinsky model ($-\cdot-$), WALE model (- - -) and ILES ($\cdots$), in comparison with DNS data ($\circ\circ\circ$) for fixed pressure gradient (left) and fixed mass flux (right).

As shown in Eq. 19, for a given distance to the wall, relative error of simulation result was determined, referenced to the *'real'* value, given by DNS data.

$$e(y^+) = \frac{|u^+(y^+) - u^+_{DNS}(y^+)|}{u^+_{DNS}(y^+)} \tag{19}$$

A similar equation could be derived for the turbulent kinetic energy. Mean error for each SGS model in each simulation was determined as the spatial averaged relative error, according to Eq. 20:

$$E_r = \frac{1}{y^+_{max} - y^+_{min}} \int_{y^+_{min}}^{y^+_{max}} e(y^+)\ \mathrm{d}y^+ \tag{20}$$

Trapezoidal rule was used in the calculation of the integral. Results of this analysis are graphically shown in Fig. 5 and Fig. 6.

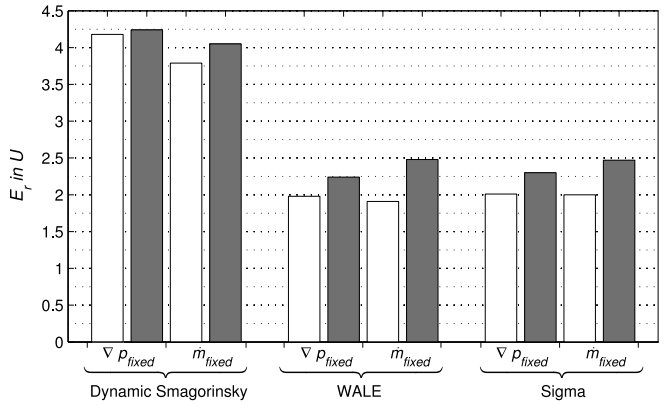

Fig. 5: Mean errors in velocity fields. Fine mesh (white); Coarse mesh (gray).

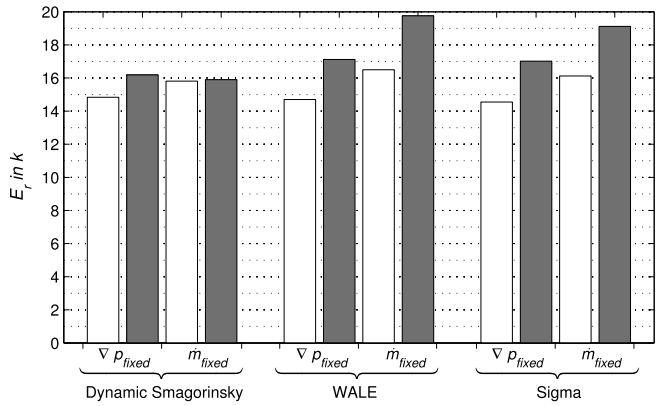

Fig. 6: Mean errors in turbulent kinetic energy. Fine mesh (white); Coarse mesh (gray).

According to the interpretation of mean velocity profiles, the Sigma and WALE models provide a much better prediction, reducing the error of the dynamic Smagorinsky model by a factor of two. A similar behavior is observed on the finer mesh as well. Fig. 5 shows that reduction of the mean error is

higher for the Sigma and WALE models, which prove to be more sensitive to mesh refinement; this is not so apparent when the dynamic Smagorinsky model is used. Fig. 6 shows that the dynamic Smagorinsky is the best model in the estimation of velocity fluctuations on a coarse mesh. However, when the mesh is very fine, the three models exhibit a very similar behavior with no significant differences.

Looking at the momentum source, a fixed pressure gradient generates a more accurate prediction of friction velocity, which is overestimated when a fixed mass flow condition is used. After non-dimensionalization of each simulation results with its own friction velocity, mean quantity errors seem to increase when using fixed mass flux for the WALE and Sigma models, with an opposite behavior for the dynamic Smagorinsky model. Conclusions on the influence of mesh resolution and SGS model apply for either of the two momentum sources.

It is widely accepted that the asymptotic behavior of the SGS viscosity in the near-wall regions is an important consideration when studying wall-resolved LES. Therefore mean ν_{SGS} behavior near the wall was computed for each model in order to check the agreement of each model to the theoretical ($\nu_{SGS} = O(y^3)$) behavior.

As it is shown in Fig. 7, the WALE model is the one which best agrees with the third-power law. The dynamic Smagorinsky model generates a proper behavior when the mesh is fine enough, with the exception of the very first grid cells. Even though the Sigma model theoretically behaves according to the third power law [2], this trend has not been captured in the simulations performed, which prove to have insufficient resolution to show the

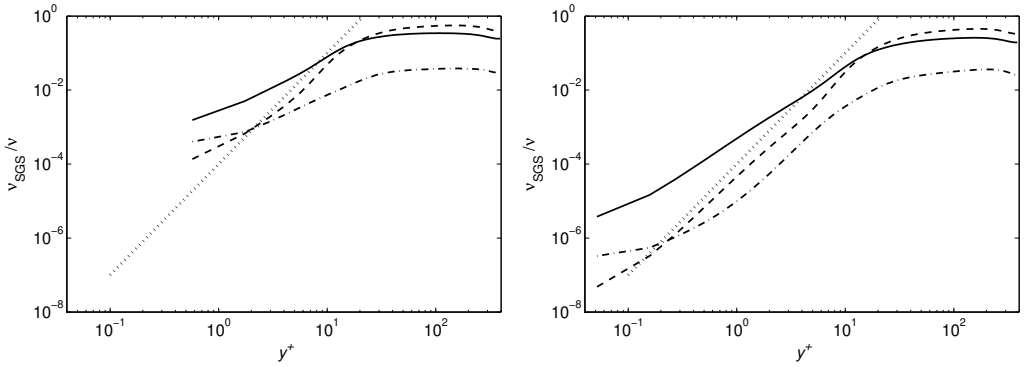

Fig. 7: Asymptotic behavior of subgrid-scale viscosity in coarse (left) and fine (right) mesh. Results are shown for static σ-model (—), dynamic Smagorinsky model ($-\cdot-$) and WALE model (- - -). Theoretical $O(y^3)$ behavior is also shown ($\cdots$).

theoretical damping of SGS viscosity in this model, at least for the second order scheme considered in the simulations.

Additionally, a statistical study was performed for the fine mesh in terms of the calculation of turbulent energy spectrum (Fig. 8) and space auto-correlation (Fig. 9) of the three velocity components in the homogeneous streamwise and spanwise directions.

It can be inferred from Fig. 8 that all models show an accumulation of turbulent energy in the small scales, which however does not significantly perturb the ensemble-average quantities that are properly determined. Two-point correlations represented in Fig. 9 show that the selected domain extension in streamwise and spanwise directions was sufficient to minimize the effect of turbulent fluctuation correlation due to periodic boundary conditions.

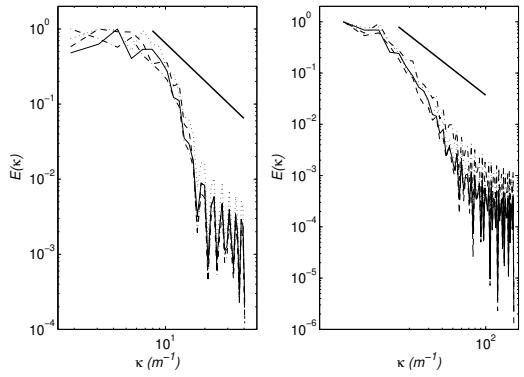

Fig. 8: Normalized turbulent energy spectrum in streamwise (left) and spanwise (right) directions. Results are shown for static σ-model (—), dynamic Smagorinsky model ($-\cdot-$), WALE model (- - -) and no-model ($\cdots$). Theoretical $-5/3$ law is also shown (**-**).

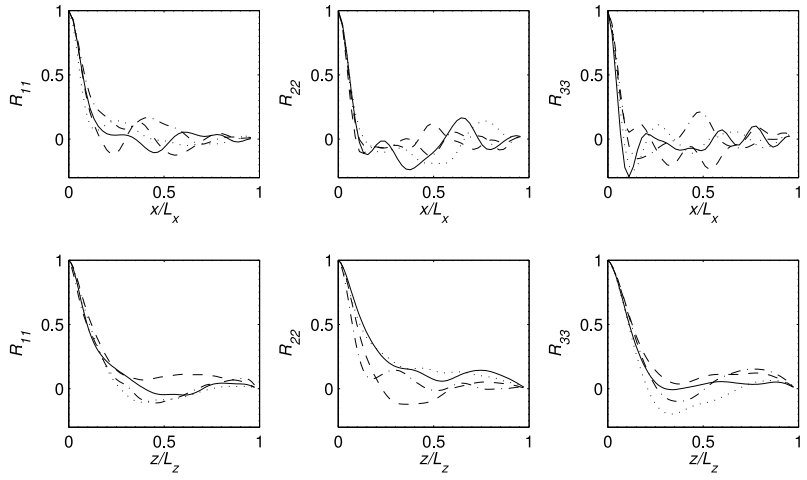

Fig. 9: Auto-correlations in streamwise (top) and spanwise (bottom) directions. Results are shown for static σ-model (—), dynamic Smagorinsky model ($-\cdot-$), WALE model (- - -) and ILES ($\cdots$).

4.2. Backward Facing Step

Numerical results on a single-sided sudden expansion geometry were compared to the experimental measurements proposed by Westphal *et al.* [40]. The experimental setup is shown in Fig. 10. Two trips were placed at the bottom and top walls (2.5 mm and 1.25 mm thick respectively) in order to generate turbulent boundary layer in the inlet channel. The inlet stream had a Reynolds number of 40,000 based on the bulk velocity at the inflow U_0 and it was fully developed at the step.

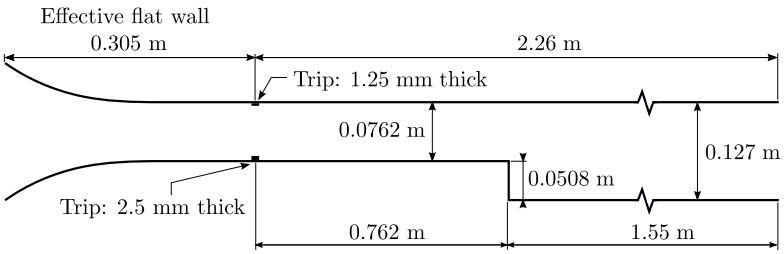

Fig. 10: Westphal *et al.* [40] experimental setup for BFS measurements.

Westphal's experimental results [40] were obtained from the combination of hot-wire and pulsed-wire anemometry measurements of mean velocity profiles and velocity fluctuations (RMS velocities). For those regions in which data was available from both methods and slightly different measurements were obtained, the following procedure was followed:

- experimental data for mean velocity profiles was obtained from pulsed-wire anemometry measurements if possible;
- for fluctuations profiles an intermediate point was selected: pulsed wire data was used in the re-circulation region up to that point and hot-wire data was used in the remaining region.

Estimated experimental errors in hot-wire anemometry data are ±2% of $U_{ref} = 12$ m/s for mean velocity profiles and up to ±4% for fluctuations profiles. Pulsed-wire experimental errors, as reported in Westphal *et al.* [40], were estimated to be lower than ±5% for mean velocity profiles and velocity fluctuations.

Pressure and friction coefficients (defined in Eq. 21) were compared to the experimental data (reference pressure p_{ref} was taken at upper wall in $x/H = -3$, where $H = 0.0508$ m is the height of the step), as well as reattachment point X_R (it was determined by looking at the change of sign in C_f).

$$C_f = \frac{\tau_w}{\frac{1}{2}\rho U_0^2}; \qquad C_p = \frac{p - p_{ref}}{\frac{1}{2}\rho U_0^2} \tag{21}$$

The simulation domain was chosen to represent only a small portion of the BFS experimental setup, as shown in Fig. 11. Inlet channel, with a height of $W_1 = 1.5H$, and a length of $L_1 = 9.75H$, was chosen to ensure fully developed flow near the step. The length of outlet channel $L_2 = 30.52H$ was large enough for the solution not to be influenced by the vicinity of outlet boundary condition.

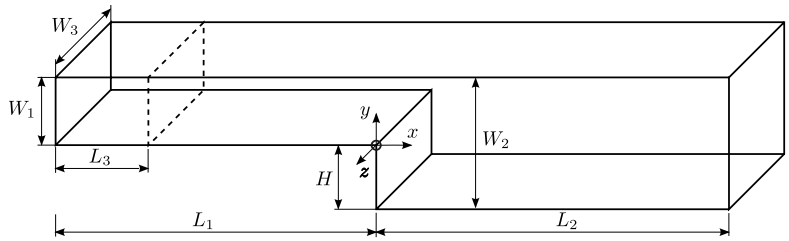

Fig. 11: Simulation domain chosen for backward facing step geometry; $L_1 = 9.75H$; $L_2 = 30.52H$; $L_3 = 4.5H$; $W_1 = 1.5H$; $W_2 = 2.5H$; $W_3 = 1.97H$.

.

Inlet boundary condition based on plane mapping was periodic for velocities. The reference plane for this condition was placed at $L_3 = 4.5H$ from the inlet, as shown in Fig. 11.

4.2.1. Computational procedure for BFS case

A fully structured cartesian orthogonal mesh was considered for this case as already selected in other studies [41]. Mesh resolution discussed in this paper was chosen on the basis of studies in Ref. [16]. Grid cell aspect ratio was kept constant in the spanwise direction. Local refinement was applied near the wall to ensure the maximum y^+ value shown in Table 4.

Table 4: Mesh resolution near the wall

Number of cells	~ 1.2 M
Δx^+_{max}	350
Δy^+_{max}	1
Δz^+_{max}	60

Spanwise direction was considered statistically homogeneous and periodic conditions were used at boundaries. Its extent was found to be sufficient to ensure non-correlation along the z-direction;

Two schemes for advection terms were considered: second-order accurate central differencing scheme `CDS` and blended `LUST` scheme (maintaining second order accuracy). In some complex meshes, pure second-order schemes are not an option (due to numerical instability), and the goal in this case is to study the influence of the choice of a blended scheme on the results for each LES model considered.

Simulations were carried out with the three SGS models described in section 3, ILES, and each of the numerical schemes shown above.

4.2.2. Results for Backward Facing Step

Mean streamwise velocity and streamwise velocity fluctuations profiles (Fig. 12 and Fig. 13), friction coefficient (Fig. 14) and pressure coefficient (Fig. 15) are shown for each combination scheme/model.

In order to estimate the error in velocity fields, 8 planes were selected in the re-circulation and recovering region (from $x/H = 2$ to $x/H = 18$). In each plane n, located at x_n, differences between simulation and experimental results were determined at each distance from the wall, and expressed in terms of a reference value of velocity (U_{ref}) as shown in Eq. 22.

$$e_n(y) = \frac{|u_{sim}(x_n, y) - u_{exp}(x_n, y)|}{U_{ref}} \tag{22}$$

This error was averaged in the height of the domain. A final mean error was determined by averaging mean errors of each of the eight planes, as shown in Eq. 23. Similar procedure was used for velocity fluctuations profiles.

$$E_r = \frac{1}{8}\sum_{n=1}^{8} \frac{1}{y_{max} - y_{min}} \int_{y_{min}}^{y_{max}} e_n(y)\mathrm{d}y \tag{23}$$

Integration was performed using the trapezoidal rule. The use of a fixed reference in the relative error determination, was chosen to give the same importance to errors near the wall (where velocities are very low) and in the middle of the channel.

For pressure and friction coefficients similar procedure was followed, averaging results in the x direction. Reference values for each variable are shown in Table 5.

Table 5: Reference values for error calculation in Backward Facing Step geometry

Variable	Reference value
U	$U_{ref} = 12\, m/s$
u_{rms}	$U_{ref} = 12\, m/s$
C_f	$C_{f,ref} = 2 \cdot 10^{-3}$
C_p	$C_{p,ref} = 0.45$

These values were chosen to be close to the maximum of each variable in experimental results.

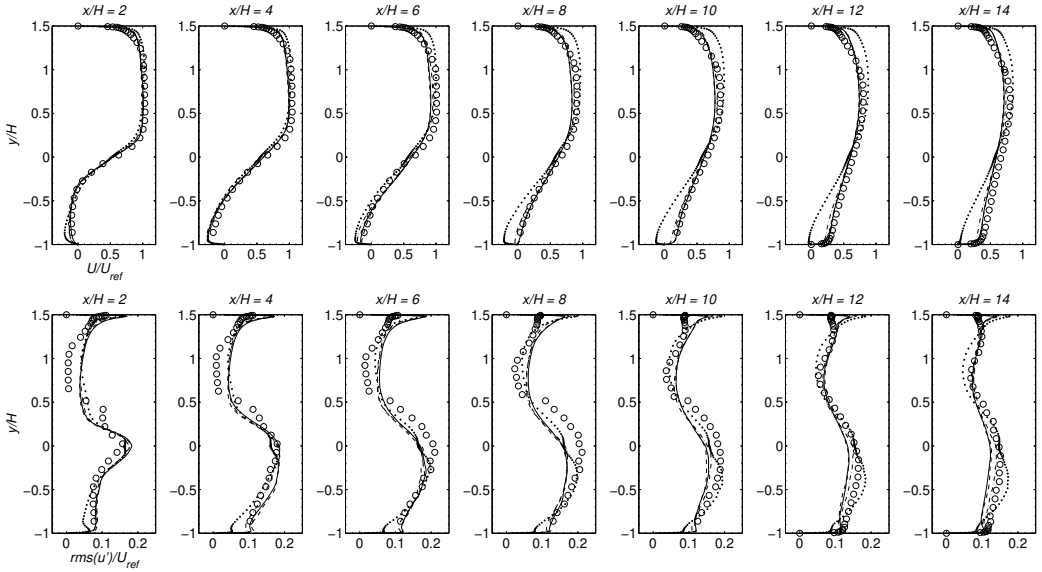

Fig. 12: Velocity (top) and RMS-velocity (bottom) profiles using `CDS` scheme: σ-model (—); dynamic Smagorinsky model ($- \cdot -$); WALE model (- - -); ILES ($\cdots$); experimental data ($\circ\ \circ\ \circ$). A non dissipative scheme as `CDS` with ILES gives wrong results as mesh resolution is far from DNS requirements.

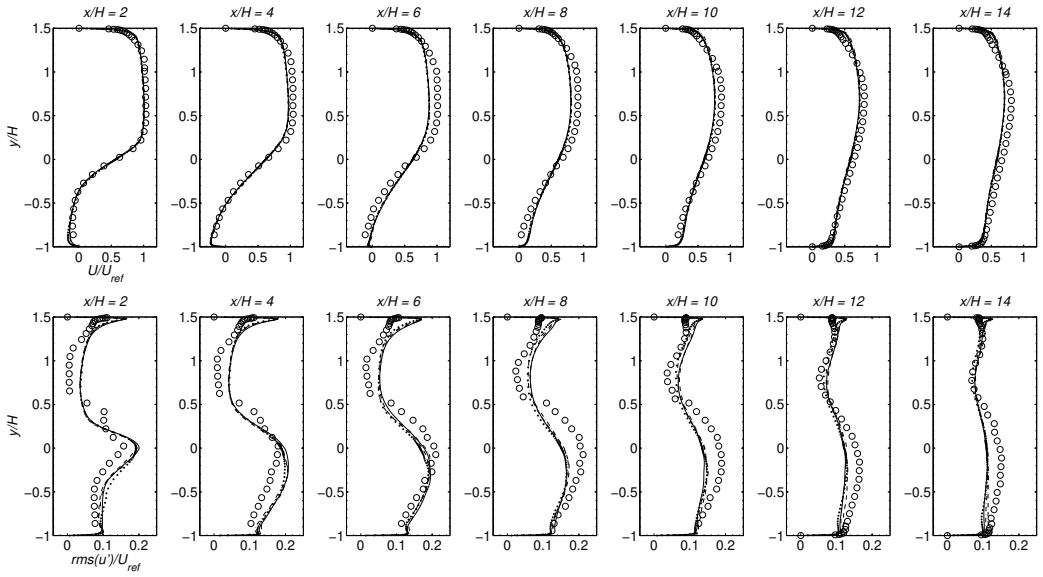

Fig. 13: Velocity (top) and RMS-velocity (bottom) profiles using `LUST` scheme: σ-model (—); dynamic Smagorinsky model ($-\cdot-$); WALE model (- - -); ILES ($\cdots$); experimental data ($\circ\circ\circ$).

As it can be inferred from Fig. 12 and Fig. 13, results for all models are in good agreement with experimental data in velocity fields and they all capture the general tendency of streamwise RMS fluctuation profiles where differences between models are more significant.

Fig. 12 demonstrates that using the implicit LES is limited to the selection of a numerically diffusive scheme (`LUST` in our case), since the use of a pure second order `CDS` leads to improper results (therefore, error analysis was not computed for this case for any variable). Considering the remaining cases, the dynamic Smagorinsky model with the `CDS` scheme yields the least error in the velocity fluctuations. It is also seen that with the `LUST` scheme,

the relative errors between the various SGS models is nearly constant.

Table 6: Average error in mean streamwise velocity profiles as a percentage of U_{ref}

Model	`CDS`	`LUST`
D. Smagorinsky	5.0299	6.2564
WALE	5.0430	5.9765
σ-model	5.0138	6.2048
ILES		5.9544

Table 7: Average error in streamwise fluctuation profiles as a percentage of U_{ref}

Model	`CDS`	`LUST`
D. Smagorinsky	1.9944	2.4912
WALE	2.4135	2.5705
σ-model	2.3755	2.7832
ILES		2.6962

As shown in Table 6 and Table 7, all mean errors obtained when using `LUST` are higher than those of the `CDS` scheme. The numerical dissipation introduced by the blended scheme is considerably larger compared to sub-scale dissipation associated with the subgrid-scale model, thus minimizing differences in the use of the WALE, Sigma or dynamic Smagorinsky models. When numerical dissipation is the only source of viscosity in sub-scale motion modeling (ILES with `LUST` scheme), results are similar to those obtained by any of the models chosen.

Wall friction coefficient calculated as explained in Eq. 21 is shown in Fig. 14 for all the simulations considered.

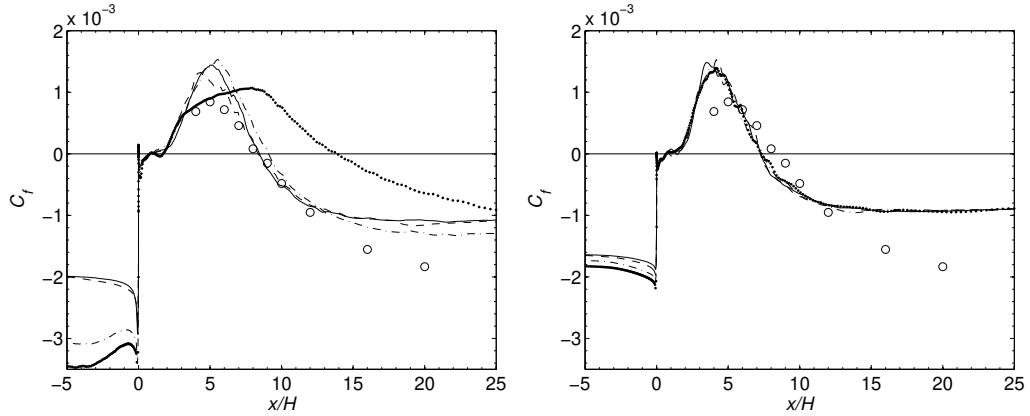

(a) (b)

Fig. 14: Friction coefficient at lower wall for `CDS` (a) and `LUST` (b) schemes: σ-model (—); dynamic Smagorinsky model ($- \cdot -$); WALE model (- - -); ILES ($\cdots$); experimental data ($\circ \circ \circ$).

The trend of C_f is qualitatively captured well under all conditions (excepting the ILES with non dissipative scheme which is considered for comparison), but some important differences exist. Fig. 14a shows that for the `CDS` scheme, the WALE model shows a better prediction of the absolute value of C_f in the vicinity of $x/H = 5$, and gives results very close to those of the Sigma model for $x/H > 7$. The dynamic Smagorinsky model gives here the least accurate results (not considering ILES), over-predicting the peak at $x/H = 5$ as well as the reattachment length. As already shown for velocity and fluctuation profiles, Fig. 14b shows that differences in estimated C_f between models are reduced when `LUST` scheme is used.

It should be noticed that all models overpredict C_f for $x/H > 10$. Increasing the length of the computational domain and near-wall resolution could reduce this discrepancy, at an increased computational cost, albeit.

However, since the models capture the extent of the re-circulating region well, the loss of accuracy in C_f can be considered as a trade-off for reduced computational cost.

The average error in friction coefficient for the `CDS` and `LUST` schemes for the various SGS models is shown in Table 8.

Table 8: Average error in friction coefficient calculation as a percentage of $C_{f,ref}$

Model	`CDS`	`LUST`
D. Smagorinsky	18.0434	21.0633
WALE	15.6739	22.1769
σ-model	17.9124	21.7687
ILES		19.6346

Friction coefficient allows the determination of the reattachment length, shown in Table 9, and its error in comparison with the experimental value of $X_R/H = 8.55$, as shown in Table 10.

Table 9: Reattachment length X_R/H

Model	`CDS`	`LUST`
D. Smagorinsky	9.0884	7.5508
WALE	8.3586	7.5770
σ	8.4546	7.3306
ILES		7.3264

Numerical dissipation introduced by `LUST` produces an under-estimation of the reattachment length significantly increasing the error in its determination. When `CDS` scheme is used, both the WALE and Sigma models generate

Table 10: Average error in reattachment length in coarse mesh as a percentage of $X_{R,ref}/H = 8.55$

Model	`CDS`	`LUST`
D. Smagorinsky	6.2976	11.6866
WALE	2.2382	11.3801
σ-model	1.1158	14.2615
ILES		14.3109

a much better prediction compared to that of the dynamic Smagorinsky model.

Impact of the SGS models and spatial discretization schemes on the pressure coefficient, as defined in Eq. 21, is discussed next.

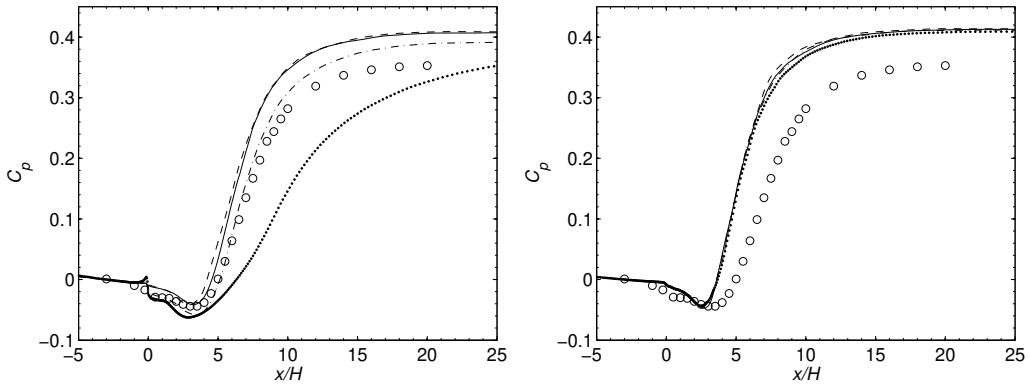

Fig. 15: Pressure coefficient at lower wall for `CDS` (left) and `LUST` (right) schemes: σ-model (—); dynamic Smagorinsky model ($-\cdot-$); WALE model (- - -); ILES ($\cdots$); experimental data ($\circ\circ\circ$).

As shown in Fig. 15, when `CDS` scheme is used, the dynamic Smagorinsky model behaves better in the prediction of pressure coefficient than the other

two, which again predict very similar results. As already shown with the rest of the parameters, the three models give a very similar prediction when a blended scheme is used.

Error analysis shown for C_p in Table 11 corroborates the above observations.

Table 11: Average error in pressure coefficient calculation as a percentage of $C_{p,ref}$

Model	`CDS`	`LUST`
D. Smagorinsky	4.5041	13.5734
WALE	10.2958	14.4385
σ-model	9.391	14.7579
ILES		14.0922

Vorticity fields were computed and results are shown in Fig. 16.

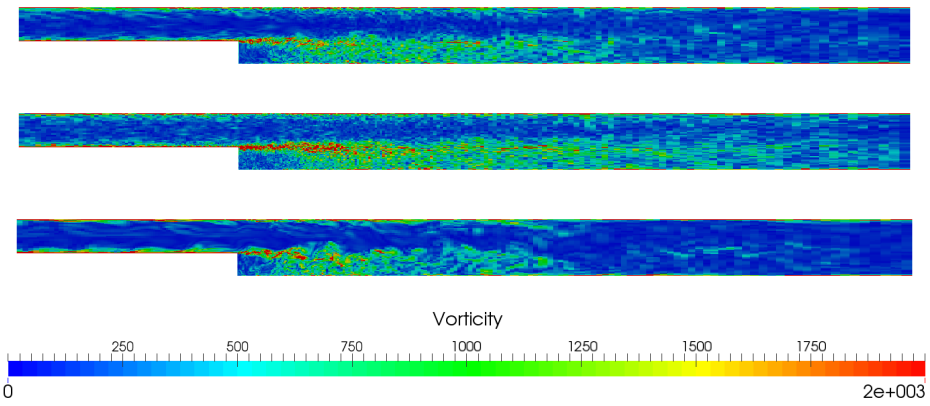

Fig. 16: Vorticity magnitude: WALE/σ-model; dynamic Smagorinsky with `CDS` scheme (center); WALE/σ-model/dynamic Smagorinsky with `LUST` scheme (bottom).

When `CDS` scheme is used, the Sigma and WALE models show a similar trend, with slightly lower vorticity magnitude when compared to the dynamic

Smagorinsky model. When the `LUST` scheme is used, all three models show approximately the same tendency, more dissipative than the previous cases.

The BFS case has highlighted the effects of numerical dissipation of the blended scheme in a perfectly orthogonal mesh. It is seen that the numerical dissipation reduces the differences between various SGS models.

It is instructive to examine the effect of the blended schemes on these SGS models in a more complex case with a non orthogonal mesh, where a central differencing scheme can no longer be used. A wall-mounted hump is chosen as a representative case for this study.

4.3. Wall-mounted hump

Turbulent separation of flow over a wall-mounted hump was studied. This flow configuration is one of the test cases considered in the NASA Workshop on Synthetic Jets and Turbulent Separation Control and it has been widely investigated [42, 43, 44]. Experimental results by Greenblatt *et al.* [45] were used as reference for model evaluation. In the experimental setup (shown in Fig. 17), boundary layer separation could be controlled by suction through a slot. However, for simplicity, the baseline case (with no suction) was selected for our work.

Reynolds number based on the free stream velocity ($U_\infty = 34.6$ m/s) and the chord length ($c = 0.42$ m) is $Re = 9.36 \times 10^5$. Two-dimensional PIV data was used along with throat dynamic pressure measurements for comparison of velocity and fluctuations profiles in the re-circulation zone, friction and pressure coefficients at the wall (reference pressure is taken at free stream at $x/H = -2.14$), and reattachment point. Several PIV sets were taken.

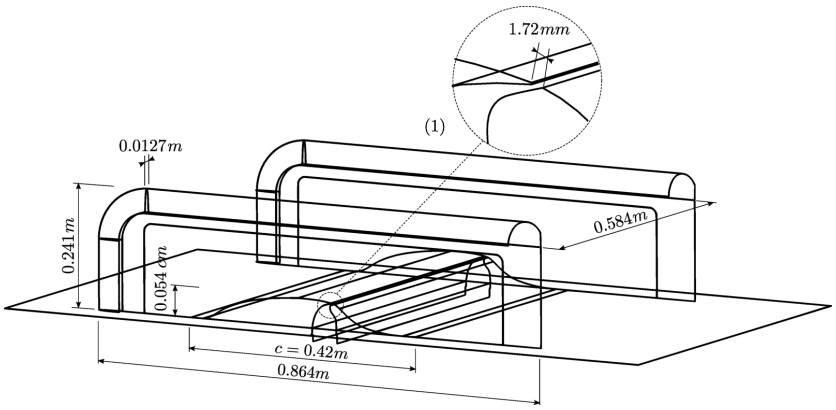

Fig. 17: Experimental model of wall-mounted hump as described by Greenblatt *et al.* [45]

.

Mean velocities errors are reported to be 2-3% precise, while RMS velocity errors are below 16%. The computational domain considered for simulations is shown in Fig 18. An upper wall is added to the domain in order to account for the blockage effect of the experimental side walls, as recommended in [45].

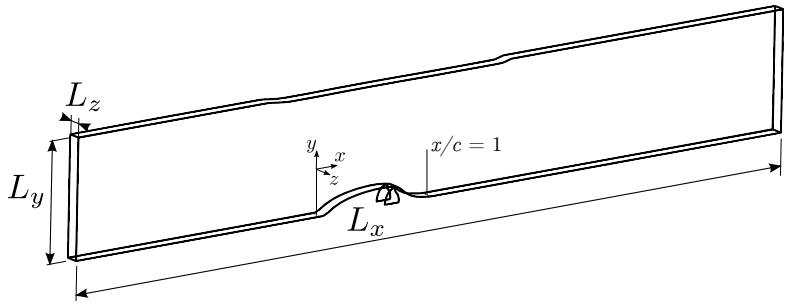

Fig. 18: Simulation domain for Hump case; $L_x = 6.14c$; $L_y = 0.91c$; $L_z = 0.2c$.

.

4.3.1. Computational procedure for Hump case

Only one mesh (a section of which is shown in Fig. 19) was generated for this case. Mesh size and quality parameters are reported in Table 12.

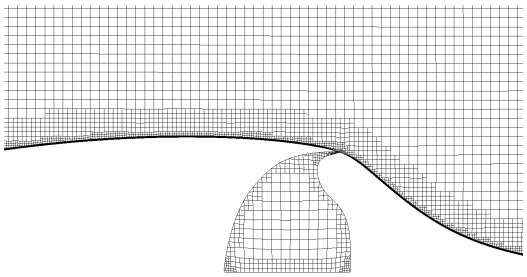

Fig. 19: Section of the mesh used for Hump case.

Table 12: Mesh characteristics for Hump case. Non-orthogonality and skewness are calculated based on their classical definitions as described in [46].

Number of cells	$\sim$ 6.66 M
Δx^+_{max}	160
Δy^+_{max}	3
Δz^+_{max}	160
Maximum non-orthogonality	44.8
Maximum skewness	1.14

Periodic boundary condition was used in the spanwise direction. The pressure was fixed at the outlet, where a zero gradient condition was applied to the velocity field. A Synthetic Turbulent Inlet condition [47] was used at the inlet of the domain. The extent of the z-direction was found to be sufficient to ensure non-correlation. All four models: WALE, σ-model, dynamic

Smagorinsky and ILES were considered using `LUST` scheme.

4.3.2. Results for hump

Profiles of velocity fields (Fig. 20) and $\overline{u'u'}$, $\overline{v'v'}$ and $\overline{u'v'}$ fluctuations (Fig. 21) in seven equidistant planes were computed.

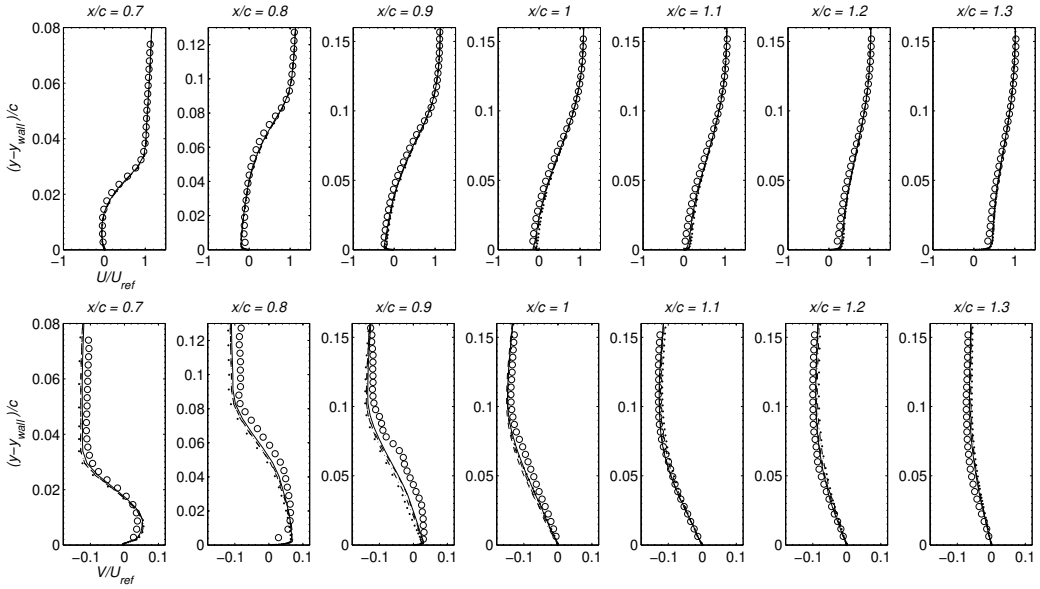

Fig. 20: Velocity field: σ-model (—); dynamic Smagorinsky model ($-\cdot-$); WALE model (- - -); ILES ($\cdots$); experimental data ($\circ\circ\circ$).

An error analysis, similar to the one proposed for the BFS problem, was performed in this case as well. Reference values for the variables considered are shown in Table 13.

Fig. 20 shows that differences between models are minimum with regards to velocity components. Fig. 21 shows that when comparing Reynolds stress tensor components differences become more noticeable. Higher differences

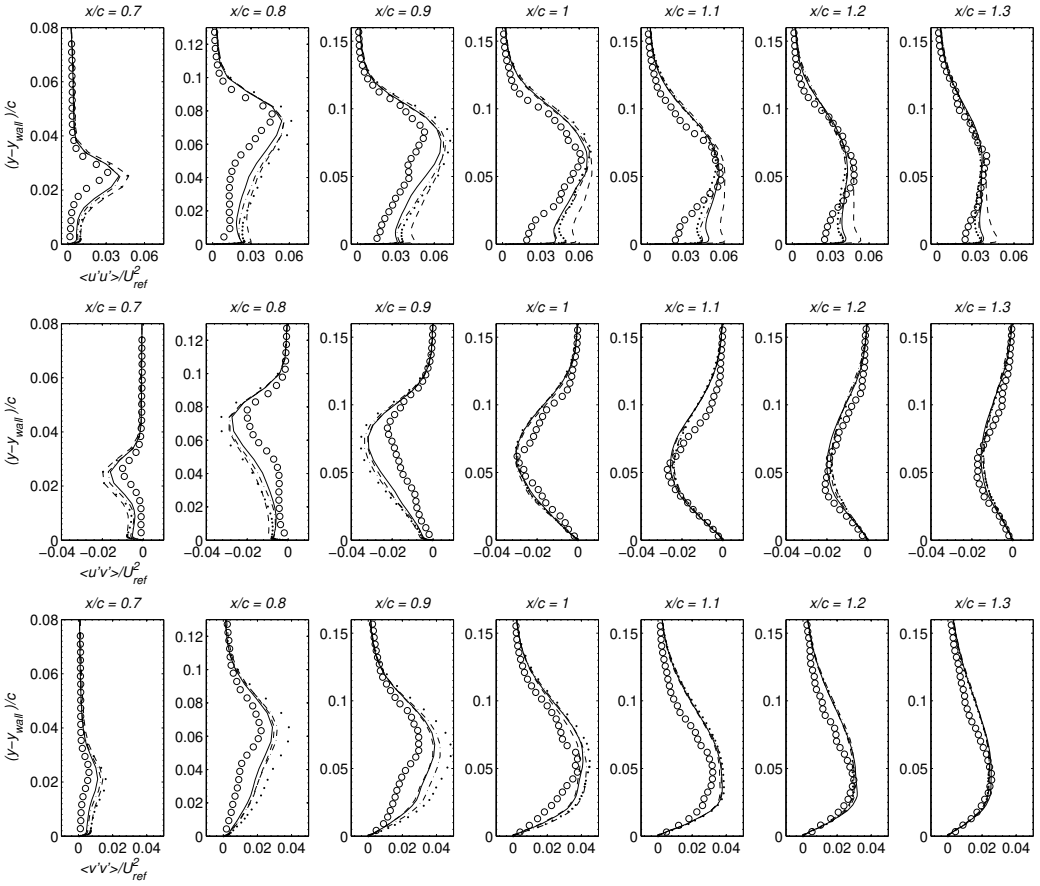

Fig. 21: $\overline{u'u'}$, $\overline{v'v'}$ and $\overline{u'v'}$ fluctuations: σ-model (—); dynamic Smagorinsky model ($- \cdot -$); WALE model (- - -); ILES ($\cdots$); experimental data ($\circ \circ \circ$).

Table 13: Reference values for error calculation in Hump geometry

Variable	Reference value
u	$U_{ref} = 34.6\, m/s$
u_{rms}	$U_{ref} = 34.6\, m/s$
C_p	$C_{p,ref} = 0.5$

are found within the re-circulation bubble (re-attachment point was experimentally found at $X_R/c = 1.11$). All SGS models tend to overpredict the peak of fluctuations (which leads to a delayed reattachment point). The Sigma model gives the best estimation in all three fluctuations considered.

Mean errors in the determination of streamwise component of velocity and $\overline{u'u'}$ fluctuations are presented in Table 14.

Table 14: Average error in streamwise velocity and $\sqrt{\overline{u'u'}}$, expressed as a percentage of U_{ref}

Model	Error in U_x	Error in $\sqrt{\overline{u'u'}}$
D. Smagorinsky	4.1201	2.5912
WALE	4.2478	3.0665
σ-model	3.4130	2.2244
ILES	4.7057	2.7587

The WALE and dynamic Smagorinsky models produce similar errors in velocity and streamwise fluctuations while the Sigma model shows the lowest discrepancy with experimental data.

Based on the friction coefficient, reattachment length has also been determined for all four models and compared to the experimental value of $X_R/c = 1.110 \pm 0.003$.

Table 15 shows excellent agreement between all models and experimental data in the prediction of the reattachment length. A maximum error of 2.13 % is seen in the dynamic Smagorinsky model whereas the Sigma model shows an error of 0.16 %.

Fig. 22 shows a comparison of the pressure coefficient obtained using

Table 15: Dimensionless reattachment length and error in its calculation as a percentage of $X_R/c = 1.110$

Model	X_R/c	Error in X_R/c
D.Smagorinsky	1.0863	2.1315
WALE	1.0933	1.504
σ-model	1.1082	0.162
ILES	1.0740	3.2460

various SGS models and experimental data. It is seen that there is excellent agreement between experimental data and numerical simulations for all the SGS models considered.

Differences between the various model predictions are negligible which can further be established by by analyzing mean errors in the determination of C_p, as shown in Table 16.

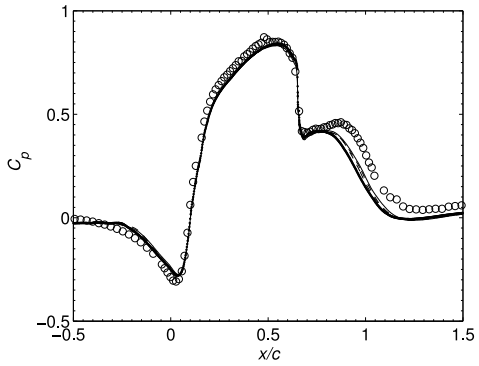

Fig. 22: Pressure coefficient at the hump surface: σ-model (—); dynamic Smagorinsky model ($- \cdot -$); WALE model (- - -); ILES ($\cdots$); experimental data ($\circ \circ \circ$).

Table 16: Average error in C_p, expressed as a percentage of $C_{p,ref}$

Model	Error in C_p
D. Smagorinsky	8.3644
WALE	8.0995
σ-model	8.2076
ILES	8.2587

The vorticity magnitude is discussed next. Since contour plots are similar for all cases only one example is examined (Fig. 23).

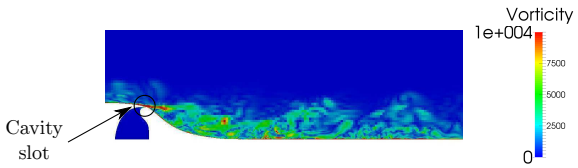

Fig. 23: Vorticity magnitude plot for simulation with σ-model.

Vorticity contours in Fig. 23 correctly depicts the separation of the turbulent boundary layer on encountering a strong adverse pressure gradient near the cavity slot. This interaction produces a large number of small scale vortices between the separated shear layer and the bottom wall. The highest values of vorticity appear in the zones near to the slot, between $x/c = 0.8$ and $x/c = 0.9$.

The main differences between experimental and simulation results appeared in the zones near to the slot. This is expected as the flow characteristics in this region are complex, since the boundary layer separates from the wall. An under-resolution of this region could explain these differences between experiment and simulations. It must be pointed out that this is a

small region compared to the rest of the domain where good agreement in velocity (Fig. 20), velocity fluctuations (Fig. 21) and pressure coefficient (Fig. 22) is observed.

4.4. Engine-like geometry: cylinder with axis-centered poppet valve

Having conducted a systematic study of flows in three canonical turbulent flow cases, we now focus on a case-study which involves a complex geometry. This geometry was chosen since it represents important flow features present in practical applications like an internal combustion engine.

As shown in Fig. 24 the geometry consists of a circular channel flow with a sudden expansion, where a poppet valve has been placed, centered with the axis of the domain, with a fixed lift of 10 mm. As a consequence a circular jet is created, generating two re-circulation regions inside the cylinder. Several studies were performed on this configuration [48, 17], since it reproduces the inlet jet flow occurring in a real engine during the induction stroke.

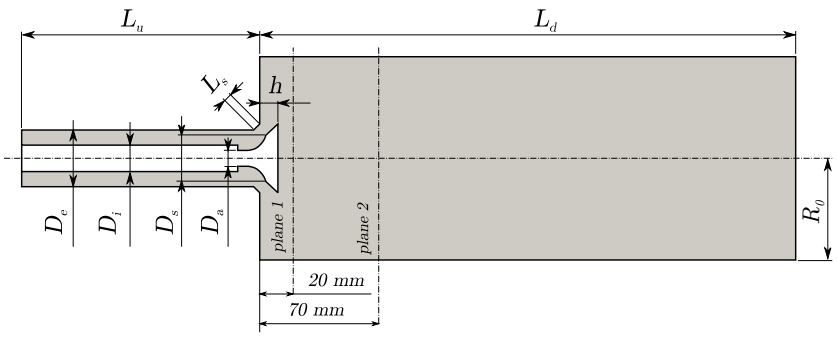

Fig. 24: Simulation domain for poppet valve case; $L_d = 300$ mm; $L_u = 138$ mm; $L_s = 4.24$ mm; $D_a = 9$ mm; $D_i = 16$ mm; $D_e = 34$ mm; $R_0 = 60$ mm; $h = 10$ mm; $D_s = 27.6$ mm;

LDA measurements [48] were obtained in this geometry with an inlet bulk velocity $U_0 = 65$ m/s, giving a mean Reynolds number of about 45,000 based

on the valve lift .

For this geometry, a grid with a total of 5.63 million grid points and Δy^+_{max} of 3 was chosen. A section of the selected grid is shown in Fig. 25. The maximum non-orthogonality of the mesh is below 55 degrees.

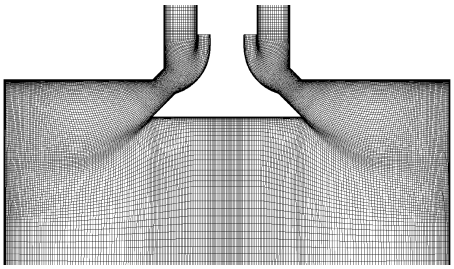

Fig. 25: Simulation grid for poppet valve case.

Given the non orthogonality of the mesh, `LUST` scheme was chosen for this case. Based on the results for the three case studies discussed earlier, the Sigma model was selected for this case. An ILES was also considered for comparison.

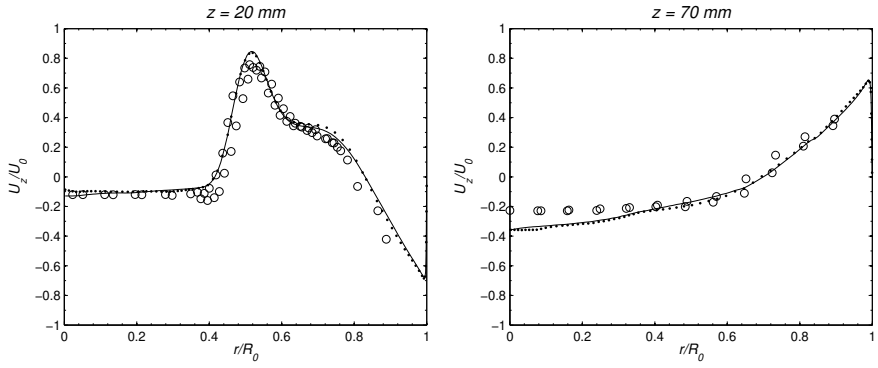

(a) (b)

Fig. 26: Axial velocity profiles: σ-model (—); ILES ($\cdots$); experimental data ($\circ\,\circ\,\circ$).

Fig. 26 shows a comparison between the mean radial and mean axial ve-

locity profiles and experimental data for two z locations, namely $z = 20$ mm (Fig. 26a) and $z = 70$ mm (Fig. 26b). Excellent agreement is seen between the velocity predictions by the Sigma model and the experimental data. No significant differences in mean velocity profiles are found when ILES results are compared to those of the Sigma model.

Radial velocity fluctuations in axial and tangential directions have also been compared to experimental values and are shown in Fig. 27.

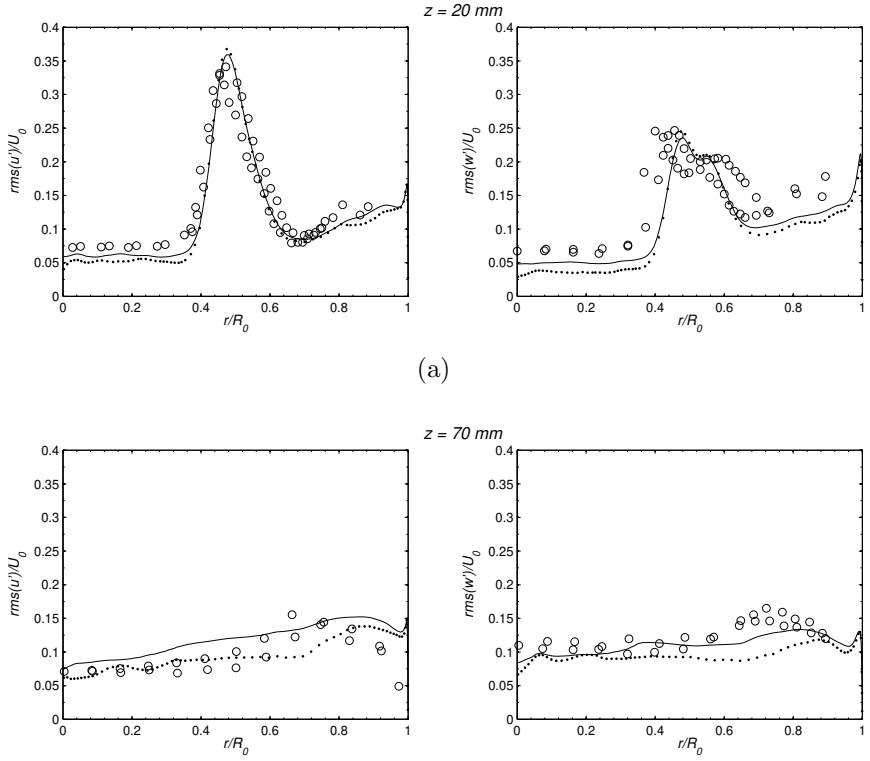

Fig. 27: Axial and tangential velocity fluctuation profiles: σ-model (—); ILES ($\cdots$); experimental data ($\circ\,\circ\,\circ$).

It is seen that axial (u') and tangential (w') velocity fluctuations at

$z = 20$ mm show very good agreement with experimental data (Fig. 27a), whereas both show good qualitative agreement at $z = 70$ mm (Fig. 27b). Differences between implicit and explicit LES become more noticeable when examining velocity fluctuations, particularly for the second experimental plane.

Results are in very good agreement with experimental data for the upper plane ($z = 20$ mm), while increasing mesh resolution near the second experimental plane ($z = 70$ mm) might be beneficial. However the satisfying agreement between simulations and experimental data shown in Fig. 26 and Fig. 27 indicates that the overall resolution used for this simulation is acceptable. For most industrial simulations involving complex geometries, qualitative trends are sufficient to guide design/development decisions. Results shown in Figs. 26 and 27 are within the acceptable limits of accuracy required for such design/development efforts.

5. Conclusions

The influence of SGS models and different numerical schemes used for spatial discretization of the advection terms on the overall accuracy of the simulation was evaluated for three different canonical turbulent flow problems. Based on the results for these canonical cases, the best combination of spatial discretization and turbulence model was used to study a practical engineering problem, namely, flow in an engine-like geometry with a centered poppet valve. The three canonical cases considered in this study were: a fully developed turbulent channel flow with $Re_\tau = 395$, a backward facing step geometry and the flow over a wall-mounted hump. An error analysis was presented to compare the performance of three SGS models, namely

Sigma (σ-model) [2] (implemented in this work in the open-source CFD code OpenFOAM®), WALE [3] and dynamic Smagorinsky [21], in the prediction of important flow characteristics: near-wall velocity profiles, velocity fluctuations and pressure and friction coefficients for some of the cases.

For the fully developed turbulent channel flow case, a second order centered differencing scheme (`CDS`) was used in two orthogonal meshes with different degrees of refinement. It was seen that the WALE and Sigma models gave the best prediction of the near-wall velocity profile, showing also a proper near-wall scaling of SGS viscosity. Both of them, giving similar results, were shown to be more sensitive to mesh resolution when compared to the dynamic Smagorinsky model.

In the BFS geometry a perfectly orthogonal mesh was used and two numerical schemes were considered in the spatial discretization of advection terms, namely, `CDS` and Linear Upwind Stabilized Transport (`LUST`). For all models the second order discretization scheme produced a lower error in the determination of all the flow characteristics considered. When the blended scheme (`LUST`) was used, the numerical dissipation introduced by the scheme was high enough to reduce the importance of the SGS model chosen. As a consequence all SGS models (an implicit LES was also considered) gave very similar results.

For the wall-mounted hump case, a non-orthogonal mesh was used and therefore, `LUST` scheme was the only option (of the two schemes proposed) in order to reach convergence. Among the three models, the Sigma model gave the best prediction of the near-wall velocity and velocity fluctuations for the case and conditions considered.

Based on its performance for the three canonical cases considered, the Sigma model was chosen together with the `LUST` scheme to study turbulent flow around a popped valve. Good agreement between experimental data and numerical simulations was observed for the mean axial velocity and velocity fluctuation profiles.

Acknowledgments

We gratefully acknowledge the computing resources provided on Blues, a high-performance computing cluster operated by the Laboratory Computing Resource Center at Argonne National Laboratory and on the HPC Facilities made available by the Fluid Dynamics Department of the Universidad Politécnica de Madrid (Madrid, Spain).

References

[1] J. H. Ferziger, M. Perič, Computational Methods for Fluid Dynamics, 3rd Edition, Springer, 2002.

[2] F. Nicoud, H. B. Toda, O. Cabrit, S. Bose, J. Lee, Using singular values to build a subgrid-scale model for large eddy simulations, Physics of Fluids 23 (8) (2011) 085106. doi:10.1063/1.3623274.

[3] F. Nicoud, F. Ducros, Subgrid-scale stress modelling based on the square of the velocity gradient tensor, Flow, Turbulence and Combustion 62 (3) (1999) 183–200. doi:10.1023/A:1009995426001.

[4] A. W. Vreman, An eddy-viscosity subgrid-scale model for shear flow:

Algebraic theory and applications, Physics of Fluids 16 (10) (2004) 3670–3671. doi:10.1063/1.1785131.

[5] J. A. Templeton, G. Medic, G. Kalitzin, An eddy-viscosity based near-wall treatment for coarse grid large-eddy simulation, Physics of Fluids 17 (10) (2005) 105101. doi:10.1063/1.2084228.

[6] U. Piomelli, Wall-layer models for large-eddy simulations, Progress in Aerospace Sciences 44 (6) (2008) 437–446. doi:10.1016/j.paerosci.2008.06.001.

[7] S. T. Bose, P. Moin, A dynamic slip boundary condition for wall-modeled large-eddy simulation, Physics of Fluids 26 (2014) 015104. doi:10.1063/1.4849535.

[8] P. Moin, J. Kim, Numerical investigation of turbulent channel flow, Journal of Fluid Mechanics 118 (1982) 341–377. doi:10.1017/S0022112082001116.

[9] D. R. Chapman, Computational aerodynamics development and outlook, AIAA Journal 17 (12) (1979) 1293–1313. doi:10.2514/3.61311.

[10] W. C. Reynolds, The potential and limitations of direct and large eddy simulations, in: J. L. Lumley (Ed.), Whither Turbulence? Turbulence at the Crossroads, Vol. 357, Springer-Verlag, 1990.

[11] P. R. Spalart, Strategies for turbulence modelling and simulations, International Journal of Heat and Fluid Flow 21 (3) (2000) 252–263. doi:10.1016/S0142-727X(00)00007-2.

[12] P. Sagaut, Large eddy simulation for incompressible flows: An introduction, 3rd Edition, Scientific Computation, Springer, 2006.

[13] H. Weller, Controlling the computational modes of the arbitrarily structured C grid, Monthly Weather Review 140 (10) (2012) 3220–3234. doi:10.1175/MWR-D-11-00221.1.

[14] A. Montorfano, F. Piscaglia, A. Onorati, A LES Study on the Evolution of Turbulent Structures in Moving Engine Geometries by an Open-Source CFD Code, SAE Technical Paper 2014-01-1147 (2014). doi:10.4271/2014-01-1147.

[15] F. Piscaglia, A. Montorfano, A. Onorati, Development of a non-reflecting boundary condition for multidimensional nonlinear duct acoustic computation, Journal of Sound and Vibration 332 (4) (2013) 922–935. doi:10.1016/j.jsv.2012.09.030.

[16] F. Piscaglia, A. Montorfano, A. Onorati, F. Brusiani, Boundary Conditions and SGS Models for LES of Wall-Bounded Separated Flows: An Application to Engine-Like Geometries, Oil and Gas Science and Technology - Rev. IFP Energies nouvelles 69 (1) (2014) 11–27. doi:10.2516/ogst/2013143.

[17] F. Piscaglia, A. Montorfano, A. Onorati, Towards the LES Simulation of IC Engines with Parallel Topologically Changing Meshes, SAE International Journal of Engines 6 (2) (2013) 926–940. doi:10.4271/2013-01-1096.

[18] F. Piscaglia, A. Montorfano, A. Onorati, Development of Fully-Automatic Parallel Algorithms for Mesh Handling in the OpenFOAM-2.2.x Technology, SAE Technical Paper 2013-24-0027 (2013). doi:10.4271/2013-24-0027.

[19] F. Piscaglia, A. Montorfano, A. Onorati, A Scale Adaptive Filtering Technique for Turbulence Modeling of Unsteady Flows in IC Engines, SAE Paper 2015-01-0395. To appear in SAE International Journal of Engines, April 2015.

[20] A. Montorfano, F. Piscaglia, A. Onorati, An extension of the dynamic mesh handling with topological changes for LES of ICE in OpenFOAM®, in proceedings of SAE 2015 World Congress & Exhibition, 2015.

[21] M. Germano, U. Piomelli, P. Moin, W. H. Cabot, A dynamic subgrid-scale eddy viscosity model, Physics of Fluids A 3 (1991) 1760–1765. doi:10.1063/1.857955.

[22] T. D. Ringler, J. Thuburn, J. B. Klemp, W. C. Skamarock, A unified approach to energy conservation and potential vorticity dynamics for arbitrarily-structured C-grids, Journal of Computational Physics 229 (9) (2010) 3065–3090. doi:10.1016/j.jcp.2009.12.007.

[23] C. Hirsch, Numerical computation of internal & external flows, 2nd Edition, B. H., 2010.

[24] S. B. Pope, Turbulent Flows, Cambridge University Press, 2000.

[25] J. Smagorinsky, General circulation experiments with the primitive equations, Montly Weather Review 91 (1963) 99–164. doi:10.1175/1520-0493(1963)091<0099:GCEWTP>2.3.CO;2.

[26] D. K. Lilly, A proposed modification of the Germano subgrid-scale closure method, Physics of Fluids A 4 (1992) 633–635. doi:10.1063/1.858280.

[27] C. Meneveau, T. S. Lund, W. H. Cabot, A Lagrangian dynamic subgrid-scale model of turbulence, Journal of Fluid Mechanics 319 (1996) 233–242. doi:10.1017/S0022112096007379.

[28] S. Ghosal, T. S. Lund, P. Moin, K. Akselvoll, A dynamic localization model for large-eddy simulation of turbulent flows, Journal of Fluid Mechanics 286 (1995) 229–255. doi:10.1017/S0022112095000711.

[29] G.-H. Cottet, A. A. Wray, Anisotropic grid-based formulas for subgrid-scale models, in: Annual Research Briefs, Center for Turbulence Research, Stanford University and NASA Ames, 1997, pp. 113–122.

[30] W. H. Cabot, Local dynamic subgrid-scale models in channel flow, in: Annual Research Briefs, Center for Turbulence Research, Stanford University and NASA Ames, 1994, pp. 143–160.

[31] D. R. Chapman, G. D. Kuhn, The limiting behavior of turbulence near a wall, Journal of Fluid Mechanics 170 (1986) 265–282. doi:10.1017/S0022112086000885.

[32] H. B. Toda, O. Cabrit, K. Truffin, G. Bruneaux, F. Nicoud, Assessment

of subgrid-scale models with a large-eddy simulation-dedicated experimental database: The pulsatile impinging jet in turbulent cross-flow, Physics of Fluids 26 (7) (2014) 075108. doi:10.1063/1.4890855.

[33] V. Moreau, I. Barton, C. Angelberger, T. Poinsot, Towards large eddy simulation in internal-combustion engines: Simulation of a compressed tumble flow, SAE Technical Paper 2004-01-1995 (2004). doi:10.4271/2004-01-1995.

[34] O. Laget, B. Reveille, L. Martinez, K. Truffin, C. Habchi, LES calculations of a four cylinder engine, SAE Technical Paper 2011-01-0832 (2011). doi:10.4271/2011-01-0832.

[35] A. Misdariis, A. Robert, O. Vermorel, S. Richard, T. Poinsot, Numerical Methods and Turbulence Modeling for LES of Piston Engines: Impact on Flow Motion and Combustion, Oil and Gas Science and Technology - Rev. IFP Energies nouvelles 69 (1) (2013) 83–105. doi:10.2516/ogst/2013121.

[36] E. Agee, A. Gluhovsky, LES model sensitivities to domains, grids and large-eddy timescales, Journal of the Atmospheric Sciences 56 (4) (1999) 599–604. doi:10.1175/1520-0469(1999)056<0599:LMSTDG>2.0.CO;2.

[37] C. H. Moeng, J. C. Wyngaard, Spectral analysis of large-eddy simulations of the convective boundary layer, Journal of the Atmospheric Sciences 45 (23) (1988) 3573–3587. doi:10.1175/1520-0469(1988)045<3573:SAOLES>2.0.CO;2.

[38] A. Misra, D. I. Pullin, A vortex-based subgrid stress model for large-eddy simulation, Physics of Fluids 9 (8) (1997) 2443–2454. doi:10.1063/1.869361.

[39] R. D. Moser, J. Kim, N. N. Mansour, Direct numerical simulation of turbulent channel flow up to $Re_\tau = 590$, Physics of Fluids 11 (4) (1999) 943–945. doi:10.1063/1.869966.

[40] R. V. Westphal, J. P. Johnston, J. K. Eaton, Experimental study of flow reattachment in a single-sided sudden expansion, Technical Report MD-41, Department of Mechanical Engineering, Stanford University, 1984.

[41] K. Akselvoll, P. Moin, Large eddy simulation of turbulent confined coanular jets and flow over a backward facing step, Technical Report TF-63, Department of Mechanical Engineering, Stanford University, 1995.

[42] V. Krishnan, K. D. Squires, J. R. Forsythe, Prediction of Separated Flow Characteristics over a Hump, AIAA Journal 44 (2) (2006) 252–262. doi:10.2514/1.13174.

[43] F. Capizzano, P. Catalano, C. Marongiu, P. L. Vitagliano, U-RANS modelling of turbulent flows controlled by synthetic jets, AIAA Journal 2005-5015 (2005). doi:10.2514/6.2005-5015.

[44] P. E. Morgan, D. P. Rizzetta, M. R. Visbal, Numerical investigation of separation control for flow over a wall-mounted hump, AIAA Journal 2004-2510 (2004). doi:10.2514/6.2004-2510.

[45] D. Greenblatt, K. B. Paschal, C. Yao, J. Harris, N. W. Schaeffler, A. E. Washburn, Experimental Investigation of Separation Control Part 1:

Baseline and Steady Suction, AIAA Journal 44 (12) (2006) 2820–2830. doi:10.2514/1.13817.

[46] F. Juretić, A. D. Gosman, Error Analysis of the Finite-Volume method with respect to mesh type, Numerical Heat Transfer, Part B: Fundamentals: An International Journal of Computation and Methodology 57 (6) (2010) 414–439. doi:10.1080/10407791003685155.

[47] L. Davidson, Hybrid LES-RANS: Inlet Boundary Conditions for Flows with Recirculation, Advances in Hybrid RASN-LES Modelling, in: Notes on Numerical Fluid Mechanics and Multidisciplinary Design 97 55–66, Springer-Verlag, 2008.

[48] L. Thobois, G. Rymer, T. Souléres, T. Poinsot, Large-eddy simulation in IC engine geometries, SAE Technical paper 2004-01-1854 (2004). doi:10.4271/2004-01-1854.